Modeling and Analysis of a Variable Speed Heat Pump for Frequency Regulation Through Direct Load Control

Citation: Kim, Young-Jin, Leslie K. Norford, and James L. Kirtley. “Modeling and Analysis of a Variable Speed Heat Pump for Frequency Regulation Through Direct Load Control.” IEEE Transactions on Power Systems 30, no. 1 (January 2015): 397–408.

Published Version: http://dx.doi.org/10.1109/TPWRS.2014.2319310

Publisher: Institute of Electrical and Electronics Engineers (IEEE)

Permanent Link: http://hdl.handle.net/1721.1/102667

Version: Author's final manuscript: final author’s manuscript post peer review, without publisher’s formatting or copy editing

Modeling and Analysis of a Variable Speed Heat Pump for Frequency Regulation through Direct Load Control

Young-Jin Kim, *Student Member, IEEE*, Leslie K. Norford, and James L. Kirtley, Jr., *Life Fellow, IEEE*

***Abstract*— This paper presents a dynamic model of a variable speed heat pump (VSHP) in a commercial building that responds to direct load control (DLC) signals, updated every 4 seconds, for the improvement of grid frequency regulation (GFR). The model is simplified for real-time simulation studies with the time horizon ranging from seconds to hours, but still sufficiently comprehensive to analyze the operational characteristics such as the heat rate and coefficient of performance. A variable speed drive-controlled induction motor model is also established for the adjustment of the VSHP input power. A dynamic model of an experimental room is then developed to estimate the effect of the DLC application to the VSHP on its indoor air temperature for two different cooling systems. Furthermore, small signal analysis is performed to evaluate both the transient response of the DLC-enabled VSHP and its contribution to GFR. Finally, with an isolated microgrid implemented with MATLAB/SIMULINK, simulation studies demonstrate that the VSHP can be effectively exploited as the DLC-enabled load while still ensuring building occupant comfort and long-term device performance.**

***Index Terms*—building occupant comfort, direct load control (DLC), grid frequency regulation (GFR), indoor air temperature, long-term device performance, small signal analysis, variable speed heat pump (VSHP).**

NOMENCLATURE

The main notations used throughout this paper are summarized here. A subscript of *hp* or *HP* represents individual or aggregated variable speed heat pumps, respectively. Furthermore, a subscript of *0* is used for steady-state variables.

A. Acronyms:

DLC	direct load control
ETP	equivalent thermal parameter
FRR	frequency regulation reserve
GFR	grid frequency regulation
HPWH	heat pump water heater
IM	induction motor
LFC	load frequency control
PFC	primary frequency control
PTC	Power/Temperature Controller
SCU	space conditioning unit
SFC	secondary frequency control
TABS	thermally activated building system
VSD	variable speed drive
VSHP	variable speed heat pump

B. Set:

t, s	time and frequency domain
ref, rated, peak	subscript for reference, rated, and peak values

C. Variable Speed Heat Pump:

P_{hp}	VSHP input power
P_m	compressor mechanical power
T_{c_amb}	condenser ambient temperature
T_{e_air}	evaporator air temperature
Q_{hp}, COP	heat rate and coefficient of performance
P_{T_ref} , Q_{T_ref} , ω_{T_ref}	scheduled reference input power, heat rate, and shaft speed for T_{air} control
ω_{hp_ref}, ω_r	reference and actual shaft speeds
$\Delta\omega_{P\_ref}$, $\Delta\omega_{T\_ref}$	reference incremental speeds for P_{hp} and T_{air} control

D. Experimental Building Room:

T_{air}, T_{adj}, T_{out}	indoor air temperature, adjacent room temperature, and outdoor temperature
T_{set}	indoor air temperature set by occupants
T_{H1}, T_{H2}, T_{L1}, T_{L2}	max. and min. limits of an acceptable temperature range with a deadband of 0.5 ^{o}C
Q_s, Q_{ig}	solar radiation and internal heat load
C	thermal capacitance
R_{cd}, R_{cv}	conductive and convective thermal resistance
L, A	thickness and area of room surfaces
c_{shc}, ρ	specific heat capacity and density of surfaces
k, h	conductive and convective heat transfer coefficients

Manuscript received November 07, 2013; revised March 01, 2014; accepted April 13, 2014. This work was supported in part by the National Science Foundation under the EFRI-SEEE Grant, Award No. 1038230. Paper no. TPWRS-01432-2013.

Y. J. Kim and J. L. Kirtley, Jr. are with the Department of Electrical Engineering and Computer Science, Massachusetts Institute of Technology, Cambridge, MA 02139, USA (e-mail: powersys@mit.edu; kirtley@mit.edu).

L. K. Norford is with the Building Technology Program, the Department of Architecture, Massachusetts Institute of Technology, Cambridge, MA 02139, USA (e-mail: lnorford@mit.edu).

ew, *iw*, *win*, *c*, *T*, *f*, *air*	subscripts for external wall, internal wall, window, ceiling, TABS, floor, and indoor air

E. Variable Speed Drive-Controlled Induction Motor:

T_{inv}, k_{inv}	variable speed drive time lag and gain
D_{hp_ref}	variable speed drive reference duty ratio
T_a, k_a	induction motor electrical time lag and gain
T_e, T_m	electromagnetic and mechanical torques
L_s, R_s	stator self-inductance and resistance
L_r, R_r	rotor self-inductance and resistance
L_m	magnetizing inductance
J, B	moment of inertia and frictional coefficient
P	number of pole pairs
λ_{ds}, λ_{qs}, λ_{dr}, λ_{qr}	*d-q* axis stator and rotor flux linkages in the synchronous rotating frame
v_{ds}, v_{qs}, i_{ds}, i_{qs}	*d-q* axis stator voltages and currents
i_{dr}, i_{qr}	*d-q* axis rotor currents
v_{dc}, i_{dc}	variable speed drive DC voltage and current
i_{abc}	induction motor three-phase input currents
ω_s, ω_{sl}	synchronous and slip frequencies
k_p, k_i	variable speed drive PI controller gains
$k_\omega(s)$	compressor load characteristics
p	differential operator, *d/dt*

F. Test Distribution Grid:

M, D	moment of inertia and load-damping constant
P_g, I_g	PI controller gains for generators
R_G, R_{HP}	droop constants for generators and VSHPs
T_g, T_t, T_{HP}	time constants of governors, turbines, and VSHPs
ΔP_G, ΔP_L, ΔP_{HP}, ΔP_{PV}	incremental power of generators, loads, VSHPs, and photovoltaic systems
ΔP_{G_max}	difference between max. and min. total ΔP_G
$P_{building\_max}$	building maximum power consumption
$\alpha_{1\text{-}5}$, α_{HP}	participation factors of generators and VSHPs
f	grid frequency
$\Delta\omega$, Δf_{rms}	frequency deviation in the unit of pu and Hz
r, x	transformer resistance and reactance
$t_{sampling}$	sampling time of $\Delta\omega$
t_d	4-second time delay
m	index of generators
n	index of grid frequency samples
N	total number of grid frequency samples

I. Introduction

GRID frequency regulation (GFR) has the intention of maintaining instantaneous balance between generation and load demand. It has been successfully undertaken at traditional generators such as coal burning, combined cycle, and hydroelectric units. However, the frequency excursion of 0.1 Hz has been caused by progressively smaller power disturbance over the last few decades [1]. In addition, the number of larger and longer-lasting frequency excursions has continuously increased even in large-scale grids such as the Eastern Interconnection of the United States [2]. In fact, the instantaneous balance has been more difficult to achieve mainly due to the increases in the penetration levels of renewable energy resources and the usages of constant power loads [3], [4]. The frequency instability might be more severe in smaller isolated grids where the moment of inertia of generation units and load damping are not sufficiently large. Consequently, conventional generation units are required to respond excessively to grid operators' commands, resulting in higher mechanical stress as well as a higher level of minimum acceptable frequency regulation reserve (FRR) capacity.

Direct load control (DLC) has been widely considered as a means of providing GFR ancillary services for financial and operational benefits to grid operators, load-serving entities, and electricity consumers [5], [6]. In particular, as communication with commercial buildings is possible via the Internet, they have been utilized as intermediate aggregators to monitor the individual loads of internally located households for DLC applications. Furthermore, the commercial buildings themselves may be regarded as end-consumers with relatively large loads, most of which are controllable under the supervision of a central load dispatching center or local control centers [7]. As an example, the power consumption of space conditioning units (SCUs) for ventilation, space cooling/heating, and water heating has been actively modulated over time in response to DLC signals [8]–[11]. In fact, commercial buildings consumed more than 35% of the total electricity in the US in 2010 [12]. The SCUs represent about 30% of electricity usage in commercial buildings, and are major drivers of summer peak loads [13]. Therefore, the DLC application to the SCUs may have significant potential to improve frequency stability.

The direct controls of the SCUs to reduce grid frequency deviation and minimum acceptable capacity of FRR have been widely studied [14]–[23]. For instance, a variety of input power control logics, mainly based on the probability distribution functions in [14] and [15] or the first-order differential equations in [16] and [17], are proposed for different types of aggregated SCUs to make reliable contributions to primary (PFC) or secondary frequency control (SFC). A specific load controller is also designed in [18] for the heat exchanges between water heaters and hydrogen systems that compensate wind turbine power fluctuation. Furthermore, in [19], the transfer function of the lumped heat pump water heater (HPWH) model is described for a supplementary load frequency control (LFC), although it only reflects the response time of the induction motors in the

HPWHs. In terms of thermal load capacities, an equivalent thermal parameter (ETP) model is used to evaluate the indoor air temperature variation due to a frequency-responsive space heating unit in [20], and especially with consideration of several device constraints in [21]. In [22], a simplified ETP model is also adopted for the analysis of temperature behaviors inside DLC-enabled refrigerators. In [23], the detailed thermal dynamics of an electric water heater are presented for the provision of minute-by-minute power regulation service. These papers consider the on-off cycle of small-size SCUs, which are used in residential buildings. Therefore, the dynamic characteristics of the physical devices in the SCUs, such as heat exchangers and thermostat controllers, as well as their transient responses to DLC signals, would not be required for the real-time GFR analysis.

DLC-enabled fans and chillers in commercial buildings have recently been analyzed [8]–[11]; however the transient variations in both the input power and heat rate need to be further investigated. For example, in [8], the input and output characteristics of the air supply fan are described without considering the duct pressure dynamics. In [9], a linearized autoregressive model of a fan, which was obtained from a specific experimental dataset, shows a relatively large discrepancy between the measured and calculated fan power consumption, especially during the transient periods. In [10] and [11], the response times and efficiencies of the fan or chiller models, which directly affect the input power variation, were assumed to be constant, regardless of the steady-state operating conditions. This may explain why the real-time GFR was not successfully implemented in [11]. In addition, the ETP models would not be appropriate for an analysis of the thermal characteristics of a commercial building room [20], and hence the occupant thermal comfort may have to be taken into account more carefully.

The heat pump (HP) compressors have evolved from single speed to variable speed units, which have noticeably increased the efficiency and market share of variable speed heat pumps (VSHPs) [24]. Therefore, as an example of the SCUs, this paper presents a dynamic model of the DLC-enabled VSHP that is simplified for real-time simulation studies but still sufficiently comprehensive to consider the operational characteristics of the VSHP. Its steady-state and transient responses are presented with respect to the compressor mechanical power and heat rate, based on a set of complicated nonlinear differential equations derived in [25] and [26]. A variable speed drive (VSD)-controlled induction motor (IM) is also modeled for the active adjustment of the mechanical power in response to the DLC signals. In addition, the dynamic thermal models of an experimental room equipped with two different cooling systems are established to estimate the indoor air temperatures for the conventional and DLC-enabled VSHPs. Furthermore, small signal analysis is developed with the transfer function of the VSD-controlled VSHP to address the feasibility and effectiveness of the DLC application in a device- and a grid-level, respectively. Finally, simulation studies are performed in MATLAB/SIMULINK to evaluate the effects of the DLC-enabled VSHP not only on building occupant comfort and long-term device performance but also on frequency deviation and FRR capacity.

II. MODELING OF A DLC-ENABLED VSHP

A. Dynamic Model of a VSHP

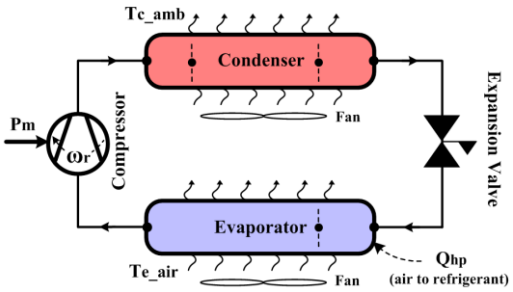

Fig. 1. Schematic diagram of a heat pump cooling cycle

As shown in Fig. 1, the main parts of a VSHP are an evaporator, a compressor, a condenser, and an expansion valve. In detail, the evaporator exchanges the heat between the air or water to be cooled and a refrigerant used as a working fluid. After the compressor raises the refrigerant temperature and pressure, the heat collected in both the evaporator and the compressor is removed from the refrigerant to the ambient air through the condenser. In the VSHP model, the input variables are defined as shaft speed ω_r, condenser ambient temperature T_{c_amb}, and evaporator air temperature T_{e_air}. Note that only ω_r is actively controllable. The output variables are compressor mechanical power P_m and heat rate Q_{hp}. In addition, the VSHP performance is evaluated using the coefficient of performance *COP*, defined as the ratio of Q_{hp} to P_m. The opening position of the expansion valve is assumed to be instantaneously controlled for the same refrigerant flow rates at the inlet and outlet of the heat exchangers. Furthermore, the fan power consumption is neglected since the majority of VSHP input power is generally used for the compression.

The input and output characteristics of the VSHP, in both transient and steady state operation, were then extracted from the coupled nonlinear differential equations presented in [25] and [26], which were based on the mass, momentum, and energy balances of the refrigerant flowing through a heat exchanger tube. Since the balances are achieved for all types of VSHPs, the generic model described in this paper may provide a basis for modeling such VSHPs. It should be noted that the differential equations have been experimentally verified in [25] and [26], particularly in terms of the long-term variations of the refrigerant temperatures.

In a steady state, where the variables are expressed with an additional subscript of *0*, P_{m0} is almost linearly dependent on ω_{r0}, T_{c_amb0}, and T_{e_air0} as shown in Fig. 2(a)–(c), respectively, which results in

$$P_{m0} = k_\omega \omega_{r0} + k_c T_{c\_amb0} + k_e T_{e\_air0} + k_{offset}. \quad (1)$$

The coefficients k_ω, k_c, k_e, and k_{offset} are determined using a multiple polynomial regressive algorithm that is applied to 2210 different combinations of the input variables over the

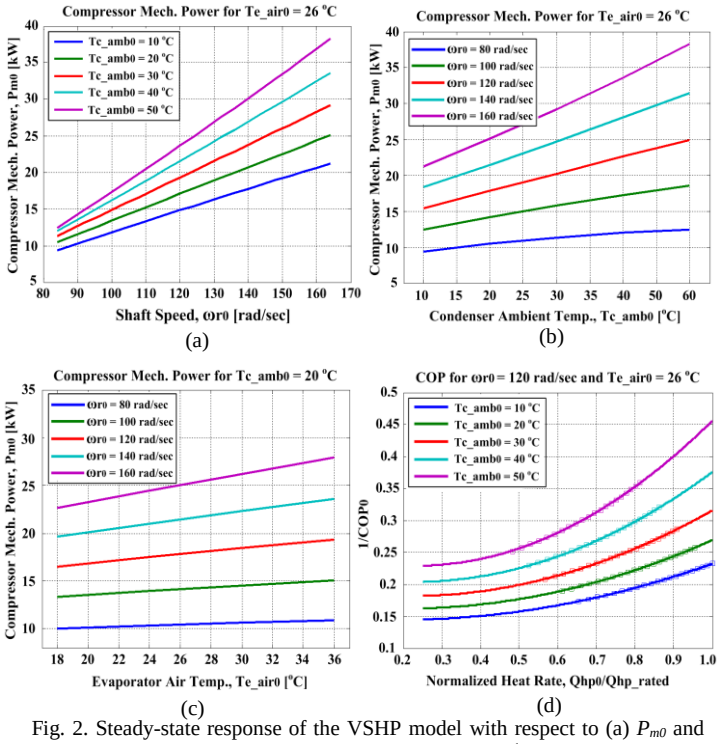

Fig. 2. Steady-state response of the VSHP model with respect to (a) P_{m0} and ω_{r0}, (b) P_{m0} and T_{c_amb0}, (c) P_{m0} and T_{e_air0}, and (d) COP_0^{-1} and Q_{hp0}

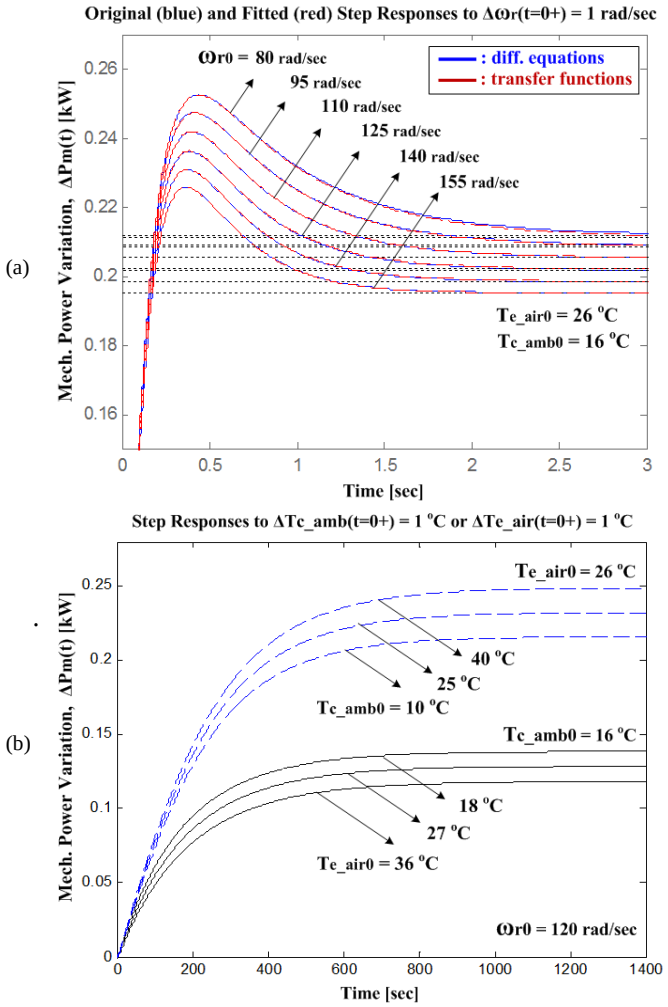

Fig. 3. Transient response of the VSHP model: $\Delta P_m(t)$ for the step increase in (a) $\Delta\omega_r(t)$, (b) $\Delta T_{c\_amb}(t)$ (blue dotted line) or $\Delta T_{e\_air}(t)$ (black line)

operating range, i.e, from ω_{r0} = 70 rad/sec to 150 rad/sec, from T_{c_amb0} = 18 °C to 36 °C, and from T_{e_air0} = 10 °C to 34 °C. The linear dependence in (1) is consistent with the specification or experimental data of the commercial VSHPs considered in [27]–[29]. Furthermore, Fig. 2(d) represents the steady-state performance map of the VSHP model, which describes the *COP* variation for normalized Q_{hp0}. It is similarly observed in the performance map of the VSHP model that is experimentally verified in [30].

In addition, for the transient response analysis, Fig. 3 shows the mechanical power variation $\Delta P_m(t)$ resulting from the step increase in the value of each input variable, i.e., for $\Delta\omega_r(t{=}0^+)$ = 1 rad/sec, $\Delta T_{c\_amb}(t{=}0^+)$ = 1 °C, or $\Delta T_{e\_air}(t{=}0^+)$ = 1 °C, for different steady-state operating conditions. In the frequency domain, $\Delta P_m(s)$ can then be approximated by the second-order transfer function of $\Delta\omega_r(s)$ and the first-order transfer functions of $\Delta T_{c\_amb}(s)$ and $\Delta T_{e\_air}(s)$. Since the time constants of the first-order transfer functions are much longer than 2 to 4 seconds when the DLC signals are expected to be updated, $\Delta P_m(s)$ can be simplified to

$$\Delta P_m(s) = \frac{n_{\omega 1}s + n_{\omega 0}}{s^2 + d_{\omega 1}s + d_{\omega 0}}\Delta\omega_r(s) \tag{2}$$

where the four coefficients $d_{\omega 1}$, $d_{\omega 0}$, $n_{\omega 1}$, and $n_{\omega 0}$ depend on the input variable values in a steady state, and hence are estimated using the polynomial regression algorithm discussed in the steady-state analysis above. In Fig. 3(a), almost no difference can be seen between the original and the fitted curves.

Finally, the time variation of the mechanical power $P_m(t) = P_{m0}+\Delta P_m(t)$ can be modeled using (1) and (2), rather than the nonlinear differential equations, with a substantial reduction of simulation time. Similarly, the steady-state and transient heat rate for $Q_{hp}(t) = Q_{hp0}+\Delta Q_{hp}(t)$ can be expressed in the same form as (1) and (2), respectively, with different coefficient values, which consequently determines the *COP* in real-time.

B. Dynamic Model of a VSD-controlled IM

For the continuous adjustment of ω_r in response to DLC signals, a VSD-controlled squirrel cage IM is modeled using an indirect torque controller with a constant rotor flux linkage [31]. Different motors and controllers may be used depending on the compressor type, size, and manufacturer; however ω_r can be controlled in a similar manner. The rated power and phase voltage of the IM are 25 kW and 460 V, respectively. The 3-phase input currents i_{abc} of the IM are sensed and then transformed into the *d-q* axis currents i_{ds} and i_{qs}. As discussed in Section III-A, the i_{qs} is changed to control the electromagnetic torque T_e and consequently the ω_r, while the i_{ds} is maintained as constant. To reduce system complexity and simulation time, the VSD is modeled with ideal voltage sources so that it operates as a hysteresis current-controlled voltage source inverter.

The speed change rate limit of a VSD-controlled motor is often chosen to prevent input over-current and DC link over-voltage during speed acceleration and deceleration, respectively. After applying arbitrary ramp rate limits of 5, 10, 20,

and 40 rad/sec/sec to the VSD-controlled VSHP model, none of the limits caused the current or voltage problems. In this paper, the rate limit was selected as 20 rad/sec/sec and equivalently as 9.2 sec/60 Hz in acceleration/deceleration time, which is comparable with those set by default in commercial VSHPs, ranging from 5.3 sec/60 Hz to 19.8 sec/60 Hz [32]–[35].

C. Dynamic Model of an Experimental Building Room

The primary objective of the VSHP is the room temperature control against outdoor temperature and internal heat gains or losses. A dynamic room model is developed to compare the indoor air temperatures controlled by the conventional and DLC-enabled VSHPs, based on the experimental room thoroughly described in [36] and [37]. Briefly, as shown in Fig. 4, it is divided into a climate room and a test room, both within a larger laboratory room where indoor temperature is maintained as almost constant. The walls consist of multiple layers of different materials including concrete, and the floor comprises a thermally activated building system (TABS), where the cooling water flows through the pipes embedded into a subfloor. The test room has lights and heat sources that simulate internal heat gains for a common office room.

A thermal network for the experimental room is modeled with MATLAB/SIMULINK using the analogy between thermal and electrical systems [38], [39]. In the analogy, thermal parameters such as thermal resistance and capacitance as well as local thermal conditions like temperature and heat gain are, respectively, converted to electrical circuit components such as resistors, capacitors, and voltage and current sources. Fig. 5(a) shows the corresponding network with a convection cooling system. The usage of the TABS for space cooling leads to the network modification as represented in Fig. 5(b). With the parameters provided in [37], the values of the conductive and convective thermal resistance R_{cd} and R_{cv}, respectively, as well as the thermal capacitance C are given as

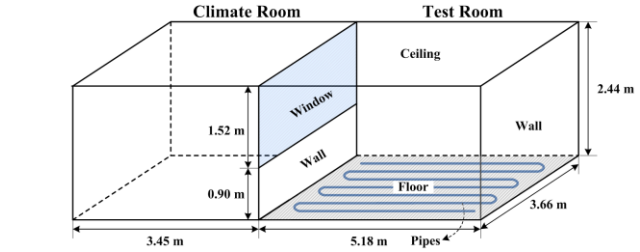

Fig. 4. Experimental room setup

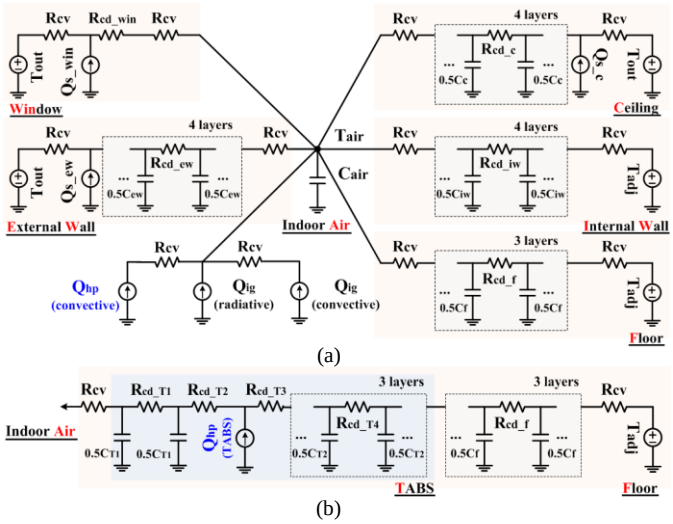

Fig. 5. Thermal networks for the experimental room equipped with different space cooling systems: (a) convection and (b) TABS

$$R_{cd} = L \cdot (k \cdot A)^{-1}, \quad R_{cv} = (h \cdot A)^{-1}, \quad \text{and} \quad C = c_{shc} \cdot L \cdot A \cdot \rho \quad (3)$$

where the L and A are the thickness and area of the room surfaces and the ρ and c_{shc} are the density and specific heat capacity of the surface materials, respectively. Furthermore,

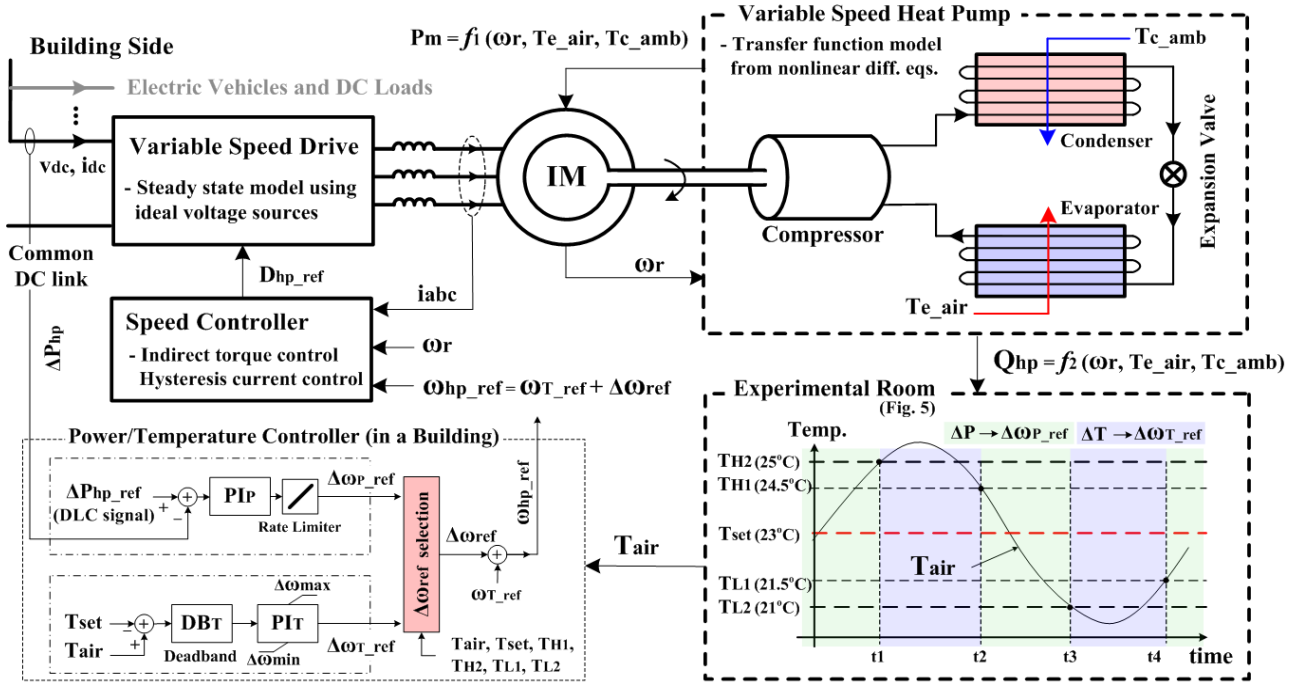

Fig. 6. A simplified schematic diagram of the VSD-controlled VSHP model for the DLC signal response and indoor air temperature control

the k and h are the conductive and convective heat transfer coefficients. In the thermal network modeling, it is assumed that the ceiling, external wall, and window receive the heat gains, proportional to their respective areas, from the solar radiation Q_s for the same outdoor ambient temperature T_{out}. The h is set to 5 W/m^{2}K, regardless of the surface characteristics, although all the convective resistors are simply denoted as R_{cv}. In addition, the combined internal heat load Q_{ig} is assumed to come equally from convective and radiative heat loads. Finally, the adjacent room temperature T_{adj} is set to constant 23 ^{o}C, which is the average temperature in the larger laboratory room.

D. Overall Dynamic Model of a DLC-enabled VSHP

All the previous models are combined for the analysis of the grid frequency and indoor air temperature controls. Fig. 6 shows the overall dynamic model of the VSD-controlled VSHP responding to the DLC signal ΔP_{hp_ref} for $T_{L2} \le T_{air} \le T_{H2}$. To enable the DLC, the upper feedback loop in the Power/ Temperature Controller (PTC) is activated to generate the $\Delta\omega_{P\_ref}$. A moving average filter is used to maintain its long-term average as close to 0 in order not to disturb T_{air}. In other words, its short-term variation does not significantly change T_{air} due to the large thermal capacity of the concrete walls and floors. For the control of T_{air}, the steady-state reference ω_{T_ref} is assumed to be scheduled based on weather forecasts one day in advance. The lower feedback loop in the PTC is activated to override the DLC for $T_{air} > T_{H2}$ or $T_{air} < T_{L2}$ due to, for example, errors in the weather forecast or unexpected changes of Q_{ig}. During the override period, or the period in which the VSHP operates at the maximum or minimum level of input power, other DLC-enabled building loads, such as electric vehicle batteries, may be used to compensate ΔP_{hp_ref}, as explained in [40]. Coordinated control of the DLC-enabled loads may be a potential method of overcoming the limits of the thermal or electrical energy storage capacities and hence reducing the occurrence of the override control, although this is not further investigated here.

III. Small Signal Analysis of DLC-enabled VSHPs

A. Input Power Control of the VSD-controlled VSHP

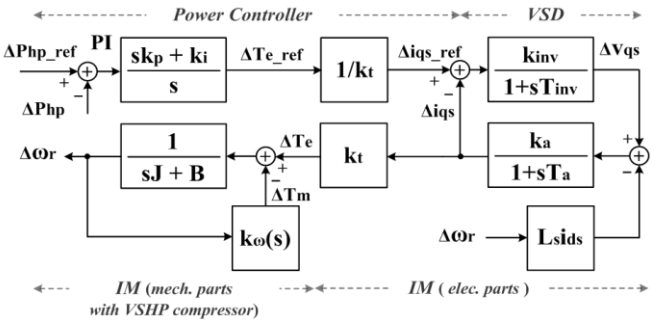

Fig. 7. Block diagram for the small-signal frequency-domain analysis of the VSD-controlled IM connected to the VSHP compressor

Fig. 7 presents the small-signal frequency-domain model of the vector-controlled IM with a constant rotor flux linkage λ_r in the synchronous rotating reference frame. In [31] and [41], the basic equations and corresponding parameters are provided for the block diagram in detail. First of all, using the flux-current relationships described in (4), the q-axis stator voltage v_{qs} is developed as (5).

$$\begin{bmatrix}\lambda_{ds}\\ \lambda_{dr}\end{bmatrix}=\begin{bmatrix}L_s & L_m\\ L_m & L_r\end{bmatrix}\begin{bmatrix}i_{ds}\\ i_{dr}\end{bmatrix},\quad \begin{bmatrix}\lambda_{qs}\\ \lambda_{qr}\end{bmatrix}=\begin{bmatrix}L_s & L_m\\ L_m & L_r\end{bmatrix}\begin{bmatrix}i_{qs}\\ i_{qr}\end{bmatrix} \tag{4}$$

$$\begin{aligned} v_{qs} &= \frac{d\lambda_{qs}}{dt}+\omega_s\lambda_{ds}+R_s i_{qs} \\ &= (R_s+L_s p)i_{qs}+\omega_s L_s i_{ds}+L_m p i_{qr}+\omega_s L_m i_{dr} \end{aligned} \tag{5}$$

If the rotor flux is placed on the d-axis, i.e., $\lambda_{dr} = \lambda_r$ and $\lambda_{qr} = 0$, the dq-axis rotor currents i_{dr} and i_{qr} are simplified to

$$i_{dr}=\frac{\lambda_r}{L_r}-\frac{L_m}{L_r}i_{ds} \quad \text{and} \quad i_{qr}=-\frac{L_m}{L_r}i_{qs}. \tag{6}$$

In the field-oriented control, the rotor current is aligned with the orthogonal axis of λ_r for effective torque production, which results in $\lambda_r = L_m i_{ds}$. Consequently, v_{qs} is expressed as

$$v_{qs}=(R_s+L_a p)i_{qs}+\omega_s L_s i_{ds}=(R_a+L_a p)i_{qs}+\omega_r L_s i_{ds} \tag{7}$$

where

$$L_a = L_s-\left(L_m^2/L_r\right), \quad R_a = R_s+\left(R_r\cdot L_s/L_r\right), \tag{8}$$

$$\text{and} \quad \omega_s=\omega_r+\omega_{sl}=\omega_r+\frac{R_r}{L_r}\cdot\frac{i_{qs}}{i_{ds}} \quad . \tag{9}$$

If the VSD power loss is negligible or constant, so that

$$P_{hp}=v_{dc}i_{dc}\cong 3\left(v_{qs}i_{qs}+v_{ds}i_{ds}\right), \tag{10}$$

the input power variation ΔP_{hp} of the VSHP is then established in the frequency domain as (11) with v_{ds} set to zero and Δv_{qs} expressed as (12).

$$\Delta P_{hp}\cong 3\left(i_{qs0}\left(R_a+sL_a\right)+v_{qs0}\right)\Delta i_{qs}+3i_{ds0}i_{qs0}L_s\Delta\omega_r \tag{11}$$

$$\Delta v_{qs}=\left(R_a+sL_a\right)\Delta i_{qs}+L_s i_{ds0}\Delta\omega_r \tag{12}$$

From (7), the Δi_{qs} is derived in the frequency domain as

$$\Delta i_{qs}=\frac{K_a}{1+sT_a}\left(\Delta v_{qs}-L_s i_{ds0}\cdot\Delta\omega_r\right) \tag{13}$$

where $k_a = 1/R_a$ and $T_a = L_a/R_a$. The time constants T_{inv} and T_a of the VSD and IM electrical parts, respectively, are normally small, which leads to $\Delta i_{qs\_ref} \approx \Delta i_{qs}$, and hence the electromagnetic torque variation ΔT_e is given as

$$\Delta T_e\cong k_t\Delta i_{qs\_ref}=\frac{sk_p+k_i}{s}\left(\Delta P_{hp\_ref}-\Delta P_{hp}\right) \tag{14}$$

where $k_t = 3P\cdot\lambda_r\cdot L_m/L_r$. In addition, $\Delta\omega_r$ is approximated by

$$\Delta\omega_r\cong\frac{1}{sJ+B+k_\omega(s)}\frac{sk_p+k_i}{s}\left(\Delta P_{hp\_ref}-\Delta P_{hp}\right). \tag{15}$$

Consequently, the closed-loop transfer function is

$$\frac{\Delta P_{hp}}{\Delta P_{hp\_ref}} \cong \frac{\left\{\left(sa_1+a_2\right)+\dfrac{a_3}{sJ+B+k_\omega(s)}\right\}}{\left(k_p+k_i/s\right)^{-1}+\left\{\left(sa_1+a_2\right)+\dfrac{a_3}{sJ+B+k_\omega(s)}\right\}} \quad (16)$$

where

$$a_1=3i_{qs0}L_a/k_t,\ a_2=3\left(v_{qs0}+i_{qs0}R_a\right)/k_t,\ \text{and}\ a_3=3i_{ds0}i_{qs0}L_s. \quad (17)$$

It is implied from (16) that the input power of the VSD-controlled IM can be actively controlled to follow the DLC signals by using appropriately large PI controller gains. This can be generally applied to VSHPs with different compressor characteristics $k_\omega(s)$, although $k_\omega(s)$ affects the variation of ω_r. Fig. 8 represents the step response of the VSD-controlled VSHP model, which operates at ω_{r0} = 100 rad/sec, T_{c_amb0} = 15 °C, and T_{e_air0} = 26 °C, to a 10-W increase in the DLC signal, i.e., $\Delta P_{hp\_ref}(t=0.05^+)$ = 10 W. Although the peak values and settling time of ΔP_{hp} depend on the steady-state operation, Fig. 8 shows that the VSD-controlled IM can respond within a short period of time so that ΔP_{hp} is adjusted to follow ΔP_{hp_ref} after approximately 0.05 seconds for the 10-W step variation.

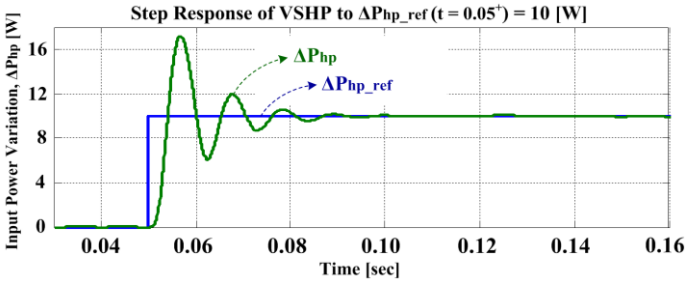

Fig. 8. Step response of the VSD-controlled VSHP to $\Delta P_{hp\_ref}(t=0.05^+)$ =10 W

B. Contribution of the DLC-enabled VSHPs to GFR

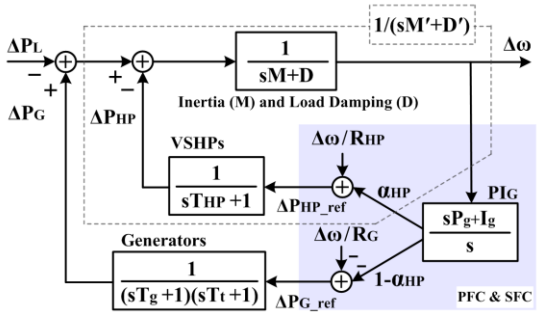

Fig. 9. Block diagram for the small-signal frequency-domain analysis of the proposed GFR in an isolated grid with a number of DLC-enabled VSHPs

Fig. 9 shows the simplified block diagram for the GFR in an isolated power grid including a number of the DLC-enabled VSHPs, denoted by *HP* in the subscript of the corresponding variables. The following conditions are considered to develop the small signal analysis of the proposed GFR:

- The GFR is achieved by adjusting the power generation and consumption of generators and VSHPs according to the reference signals ΔP_{G_ref} and ΔP_{HP_ref}, respectively.
- The reference signals consist of two components, which correspond to PFC and SFC. One is produced at the locations where the individual units are connected to the grid. The other is centrally generated and distributed from a grid operator to central or local load dispatching centers through communications links to shift the grid frequency deviation $\Delta\omega$ toward zero.
- The total accumulated dynamic response of the generators is represented by the second-order transfer function [42].
- The first-order response of the accumulated VSHPs, which are distributed over a wide range of locations, is attributed to random time delays in the communications links [43],[44].
- The PI controllers are commonly adopted for the SFC in real power grids [45].
- The VSHPs and the generators are controlled by the same PI controller with the different output ratios of α_{HP} and 1-α_{HP}, respectively. The usage of separate controllers does not significantly change the following analysis.
- Due to the inherent characteristics of the rotary pumps similar to the generators, the VSHPs contribute to the SFC in the similar, relatively low, frequency range.

In response to the load demand variation ΔP_L, the $\Delta\omega$ is then represented as

$$\frac{\Delta\omega}{\Delta P_L}=\frac{-1}{\left(sM+D\right)+g(s)+\alpha_{HP}h(s)} \quad (18)$$

where

$$g(s)=\frac{1}{R_{HP}\left(sT_{HP}+1\right)}+\frac{s\left(R_GP_g+1\right)+R_GI_g}{sR_G\left(sT_g+1\right)\left(sT_t+1\right)}, \quad (19)$$

$$h(s)=\frac{sP_g+I_g}{s}\left\{\frac{1}{sT_{HP}+1}-\frac{1}{\left(sT_g+1\right)\left(sT_t+1\right)}\right\}. \quad (20)$$

It is described in (18)–(20) that $\Delta\omega$ is reduced mainly by the supplementary PFC, characterized by the droop constant R_{HP} in (19), of the DLC-enabled VSHPs. Furthermore, since they are capable of responding faster than conventional generators, $\Delta\omega$ is additionally decreased by the SFC, i.e., for the case of α_{HP} > 0, as implied in (20). The reduction of $\Delta\omega$ is also explained with (21), which shows the increases in both the total inertia and load damping constants M and D, respectively, as follows:

$$M's+D' \cong \left(M+\frac{a_4}{s\left(sT_{HP}+1\right)}\right)s+\left(D+\frac{a_5}{s\left(sT_{HP}+1\right)}\right) \quad (21)$$

where $a_4=\left(R_{HP}^{-1}+\alpha_{HP}P_g\right)$ and $a_5=\alpha_{HP}I_g$. It indicates that the VSHPs contribute to the increases in M and D with time delays, especially in the low-frequency region. Based on (21), Fig. 10 compares the Bode plots of the open-loop transfer functions 1/(Ms+D) and 1/($M's$ + D') in the conventional and proposed GFR methods, respectively, with respect to α_{HP}. It consistently shows that the VSHPs can effectively reduce $\Delta\omega$ arising from the imbalance between ΔP_G and ΔP_L, especially for s less than the cut-off frequency $s_c = j|D'/M'|$. It needs to

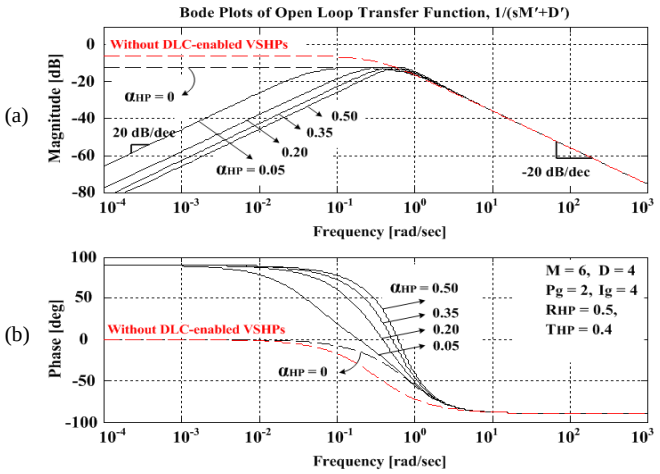

Fig. 10. Bode plot diagram of the open-loop transfer function $1/(M's + D')$ for the parameter values expressed in per unit

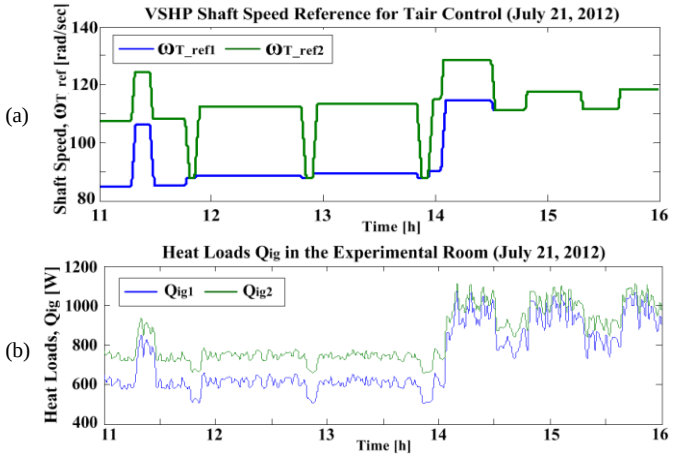

Fig. 11. (a) Steady-state shaft speed references ω_{T_ref1} and ω_{T_ref2}, and (b) corresponding internal heat loads Q_{ig1} and Q_{ig2}

be noted that D' is approximately equal to $(D+1/R_{HP})$ for $\alpha_{HP} = 0$, which mainly limits the peak values of $|1/(M's + D')|$ for $\alpha_{HP} > 0$. For $s > s_c$, the two open-loop transfer functions represent the same characteristics, regardless of α_{HP}, as shown in Fig. 10(a). This implies the advantages of frequency-responsive load devices having faster time responses, such as electric vehicles, in the reduction of $\Delta\omega$ in the high-frequency region.

In addition, the dynamic response of ΔP_G is given as (22),

$$\frac{\Delta P_G}{\Delta P_L} = \frac{m(s)\left\{R_G^{-1} + r(s)\left(1-\alpha_{HP}\right)\right\}}{(sM+D)+g(s)+\alpha_{HP}h(s)} \tag{22}$$

which results in

$$\left|\frac{\Delta P_G}{\Delta P_L}\right| \geq \frac{\left|m(s)r(s)\right|(1-\alpha_{HP})}{\left|(sM+D)+g(s)\right|+\alpha_{HP}\left|h(s)\right|} \tag{23}$$

where $m(s) = 1/\{(sT_g+1)(sT_g+1)\}$ and $r(s) = (sP_g + I_g)/s$. It is implied from (23) that the minimum required FRR capacity of the generators is almost linearly reduced with the increase in α_{HP}, especially for the small difference between the time constants of the VSHPs and generators, i.e., $|h(s)| << 1$. In this paper, the minimum required FRR capacity is defined as the difference between the maximum and minimum values of ΔP_G for a certain time period under no-fault grid conditions; i.e., grid frequency is maintained at 60 ± 0.05 Hz. Furthermore, the larger the $|h(s)|$ is, the larger the $\partial|\Delta P_G/\Delta P_L|/\partial\alpha_{HP}$ becomes for smaller α_{HP}. In other words, the VSHPs with faster time responses reduce a larger amount of the minimum required FRR capacity in their earlier adoption of the DLC.

IV. Case Studies and Simulation Results

A. Test System and Simulation Conditions

The input power of conventional HPs in a real test building at Boston University was measured with a sampling time of 1 minute on July 21, 2012 [46]. This was linearly interpolated and then scaled down to match with the rated power of the VSHP model, i.e., 25 kW, for use as the scheduled reference input power P_{T_ref} for temperature control. P_{T_ref} was assumed to vary between approximately 60% and 90% of the VSHP rated power over 5 hours. A scaled fraction of the corresponding Q_{T_ref} was then used to control T_{air} in the experimental room, and hence its variation was assumed to have a negligible effect on T_{e_air}, which was set to constant 26 °C. Two different ω_{T_ref} schedules and corresponding Q_{ig} profiles for $T_{L2} \leq T_{air} \leq T_{H2}$ were then decided as shown in Figs. 11(a) and (b), respect-ively, not only with regard to P_{T_ref} and Q_{T_ref} determined above, but also to T_{out} and Q_s obtained from [47]. It needs to be noted that ω_{T_ref} is constant at least during the 1-minute sampling time, except for the transition periods.

As shown in Fig. 12, the DLC-enabled VSHP model was tested on the IEEE 34 Node Test Feeder, modified based on [40] and [48]–[50], whose detailed specifications are presented in Table I. For simplicity, it is assumed that there are two different types of commercial buildings according to the building loads including the VSHPs, whose steady-state input power is determined by the set of ω_{T_ref} and Q_{ig}. The load demand of each type of building is then scaled up so that the blue points for the $Bldgs_1$ and $Bldgs_2$ in Fig. 12 represent a group of the commercial buildings having the same load demand profiles.

Finally, Fig. 14 describes a detailed block diagram of the proposed GFR scheme with nonlinear signal processing functionality. A grid operator is assumed to have the information on the scheduled power generation and consumption of the DGs and VSHPs, respectively, and then determines R_G, R_{HP} and $\alpha_{1\text{-}5}$. For simplicity, the DLC signals ΔP_{HP_ref}, which are updated every 4 seconds through the SFC, are assumed to be equally divided by the number of the VSHPs for $|\Delta P_{hp\_ref}| \leq$ 5 kW. The ΔP_{hp_ref} represents the signals that have been passed through continuous low-pass filters to generate $\Delta\omega_{P\_ref}$ for

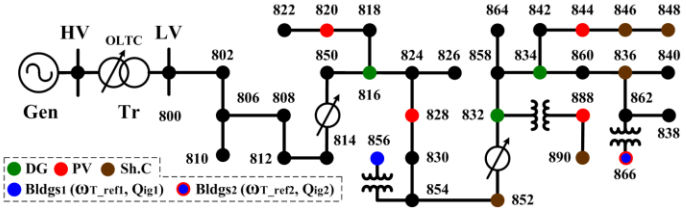

Fig. 12. Single-line diagram of the test distribution system

TABLE I. DETAILED SPECIFICATIONS OF THE TEST SYSTEM

DGs	· HV side: P_{rated} = 15 MW to compensate 5-minute load variation · LV side: P_{rated} = 3.5 MW (816), 2.5MW (832), and 3.0 MW (834)
PV	Total P_{peak} = 1 MW as the scaled-up output of the PV generators designed in [40] for the solar insolation from [47]
Loads	Balanced loads from 16.80 MW to 18.72 MW reflecting the scaled-up RegD signals in [48], as shown in Fig. 13 (0.85 pf lag)
Bldgs	$P_{buildinq\_max}$ = 530 kW, including P_{hp_rated} = 100 kW (25 kW × 4), of an individual building in $Bldgs_1$ (856) or $Bldgs_2$ (866)
Tr	· 3-phase, 115/69 kV, 25 MVA, x = 8%, x/r = 20 · On-load tap changer for -10% to +10% voltage regulation
Sh.Cs	· 1.5 Mvar each for (836), (848), and (890) · 1 Mvar each for (846) and (852)
D/Ls	Balanced line impedances adopted from the average values of each line configuration in [49]

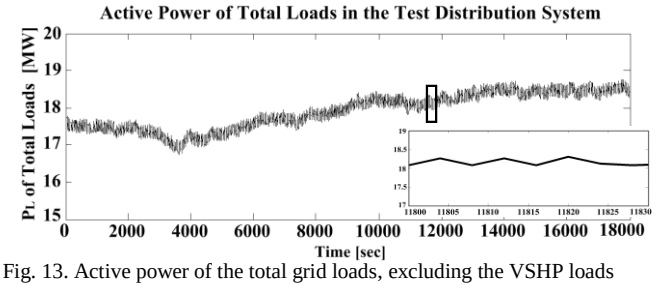

Fig. 13. Active power of the total grid loads, excluding the VSHP loads

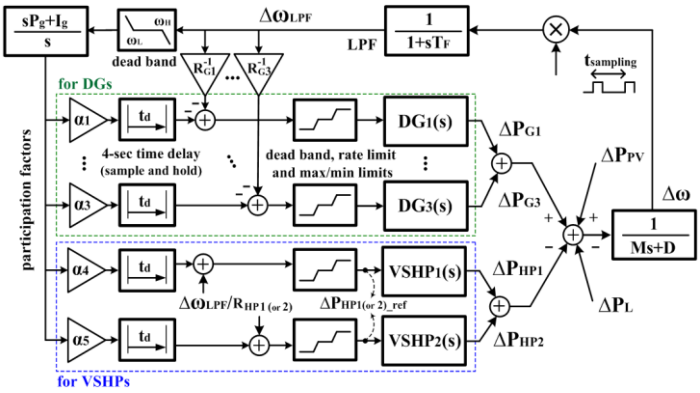

Fig. 14. Block diagram of the proposed GFR for the test distribution system

individual VSHPs in $Bldgs_1$ and $Bldgs_2$. The $\Delta\omega_{P\_ref}$ is then added to ω_{T_ref}, as shown in Fig. 6. Note that the distributed generators (DGs) at the HV and LV sides compensate the 5-minute and real-time load variations, respectively, and are modeled with the second-order transfer functions with the parameter values used in [42] and [51].

B. Simulation Results in the Experimental Room

As represented in Fig. 15, the DLC-enabled VSHP input power P_{hp} can be actively controlled in response to the changes in P_{hp_ref}. The fast response of the VSD-controlled IM, discussed in Section III-A, results in only slight differences between P_{hp} and P_{hp_ref}, especially when the VSHPs contribute to the GFR in the low-frequency range, as considered in Section III-B. In addition, ω_r was continuously adjusted in the vicinity of ω_{T_ref}, as shown in Fig. 16. Both the moment of inertia J and compressor characteristics $k_\omega(s)$ of the VSHP model affect the time delay between ω_{hp_ref} and ω_r, which is small, as described in Figs. 16(c) and (d), due to not only the small value of J but also the low-pass-filtered ΔP_{hp_ref}. The high-frequency components of ω_{hp_ref} were caused mainly by the IM input current harmonics, and were filtered out in ω_r.

Fig. 17 represents the indoor air temperatures controlled by the conventional and DLC-enabled VSHPs for the convection and TABS cooling methods. The short-term variation $\Delta\omega_r$ does not significantly affect the temperatures, especially for the TABS that includes the additional thermal capacitance in the subfloor. The negligible difference can be seen between the convection-cooled indoor temperatures, and the two curves for the TABS-cooled temperatures differ only imperceptibly. This implies that the building concrete walls and floors play the role of a low-pass filter with a substantial time constant.

Furthermore, Table II lists a comparison of the 5-hour average values of the P_{hp}, Q_{hp}, and *COP* of the conventional and DLC-enabled VSHPs with respect to ω_{T_ref}. The DLC application does not make a significant difference in the long-term performance of the VSHP. Consequently, the VSHPs can be utilized as demand response resources for the real-time GFR through the DLC while ensuring the building occupant comfort and the long-term device performance.

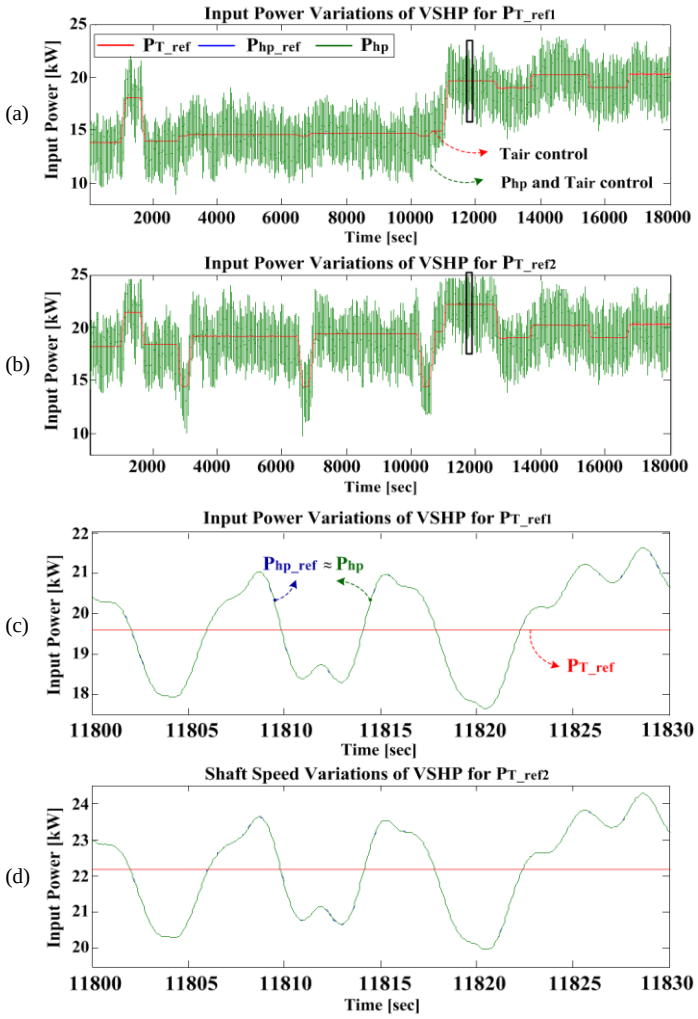

Fig. 15. Input power variations of the VSHPs for (a) P_{T_ref1} and (b) P_{T_ref2} with (c) and (d) close-up plots for a period of 30 seconds

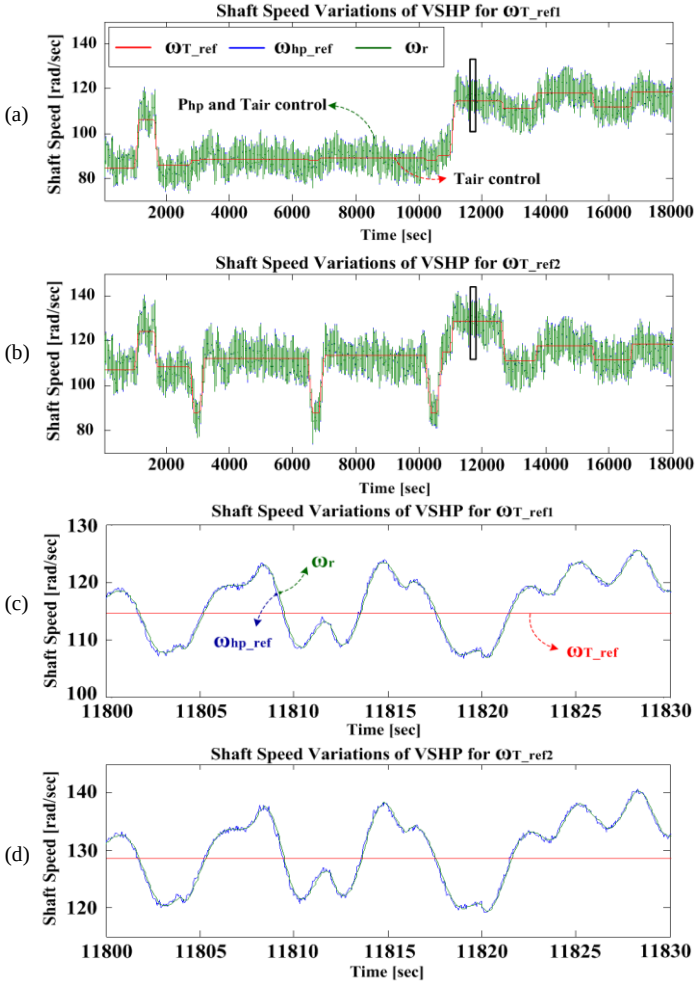

Fig. 16. Shaft speed variations of the VSHPs for (a) ω_{T_ref1} and (b) ω_{T_ref2} with (c) and (d) close-up plots for a period of 30 seconds

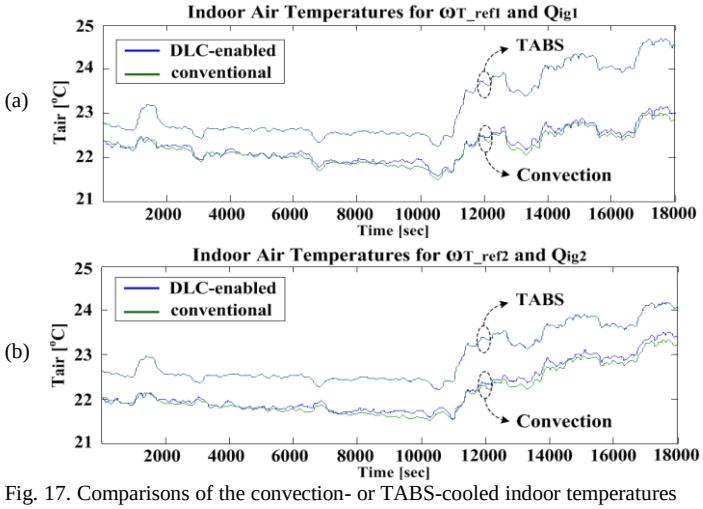

Fig. 17. Comparisons of the convection- or TABS-cooled indoor temperatures for the conventional and DLC-enabled VSHPs with (a) ω_{T_ref1} and (b) ω_{T_ref2}

TABLE II. COMPARISONS OF 5-HOUR AVERAGE OF P_{hp}, Q_{hp}, AND *COP*

VSHP Operation		P_{hp} [kW]	Q_{hp} [kW]	*COP*
ω_{T_ref1}	DLC-enabled	15.04	68.72	5.62
	Conventional	15.07	68.81	5.60
	|Diff.| [%]	0.20	0.13	0.36
ω_{T_ref2}	DLC-enabled	17.48	75.96	5.20
	Conventional	17.55	76.17	5.18
	|Diff.| [%]	0.40	0.28	0.39

C. Simulation Results in the Test Distribution System

For the analysis of the proposed GFR with respect to grid operation, Fig. 18(a) and (b) show the frequency deviation Δf_{rms} and the maximum DG output variation ΔP_{G_max}, respectively, for the different values of R_{HP} and α_{HP}. For α_{HP} = 0, the DLC-enabled VSHPs contribute only to the PFC, which does not necessarily require communications links between grid operators and commercial buildings. As α_{HP} increases, the conventional VSHPs are correspondingly converted to the DLC-enabled units contributing to the SFC while maintaining the same total amount of the VSHP loads for temperature control. The DG parameter values also remain unchanged. In Fig. 18(a), Δf_{rms} is effectively reduced through the droop control of the VSHPs. The slight reduction is also observed with the increase in α_{HP}, which implies that the response time of the VSHP is a little faster than those of the DGs. Fig 18(b) describes the linearly descending trends of ΔP_{G_max} with the increase in α_{HP}, although the synchronized load variations of different number of the DLC-enabled VSHPs led to the rather complicated results. In particular, ΔP_{G_max} decreases by about 15% even for α_{HP} = 0. Fig. 18 can be consistently explained by the small signal analysis, which is developed based on the total response of the accumulated generators and VSHPs in Section III.

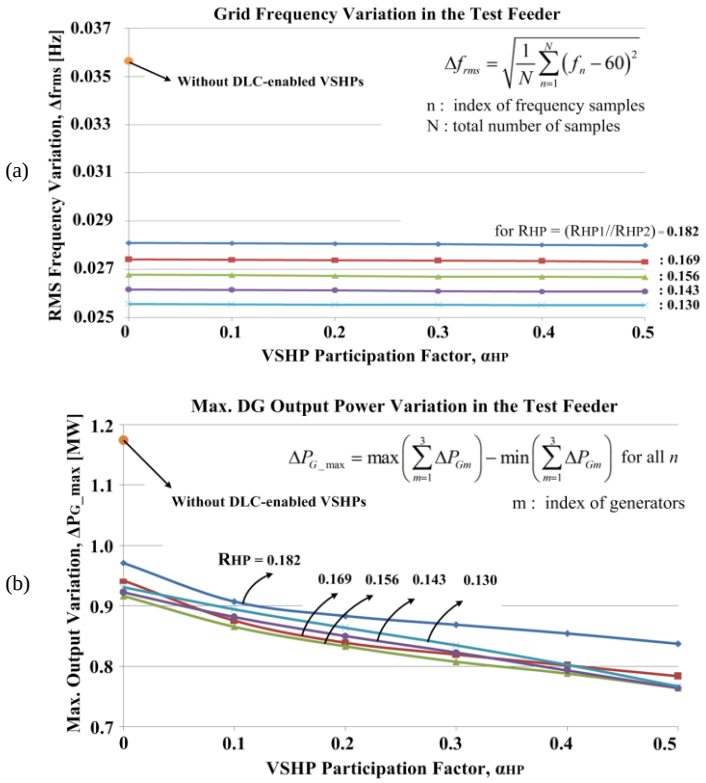

Fig. 18. (a) Δf_{rms} and (b) ΔP_{G_max} in the test distribution system due to the proposed GFR with respect to the changes of R_{HP} and α_{HP}

V. CONCLUSION

The paper presents a dynamic model of a VSD-controlled VSHP responding to the DLC signals and controlling the

indoor air temperature. Based on the nonlinear differential equations derived in the previous literature, it has been developed in an operational level as a dynamic model that is simplified for real-time simulation studies but still sufficiently comprehensive to show the relationships between the input variables ω_r, T_{c_amb}, and T_{e_air} and the output variables P_m, Q_{hp}, and *COP*. The VSHP compressor is then connected to a VSD-controlled IM whose shaft speed is adjusted by an indirect torque controller in response to the DLC signals updated every 4 seconds. To estimate the effect of the DLC-enabled VSHP on the indoor air temperature, a test room model using a convection or TABS cooling method has been established based on the experimental setup. The small signal analysis represents that the DLC can be generally applied to the VSHPs, regardless of their compressor characteristics. It also proves that the frequency deviation and generator output variation are effectively reduced through the supplementary PFC and SFC of the VSHPs. The simulation studies performed in an isolated microgrid verify that the DLC application to the VSHPs improves the frequency stability while ensuring both the occupant comfort and the long-term device performance.

REFERENCES

[1] "Frequency response standard whitepaper", Frequency Task Force of the NERC Resources Subcommittee, Apr. 2004, [Online]. Available: www.nerc.com/docs/oc/rs/Frequency_Response_White_Paper.pdf

[2] M. A. Hanley, "Frequency instability problems in North American Interconnections," National Energy Technology Laboratory (DOE/ NETL-2011/1473), May 2011.

[3] P. Sørensen, N. A. Cutululis, A. V. Rodríguez, L. E. Jensen, J. Hjerrild, M. H. Donovan, and H. Madsen, "Power fluctuations from large wind farms," *IEEE Trans. Power Syst.*, vol. 22, no. 3, pp. 958-965, Aug. 2007.

[4] H. Huang and F. Li, "Sensitivity analysis of load-damping characteristic in power system frequency regulation," *IEEE Trans. Power Syst.*, vol. 28, no. 2, pp. 1324-1335, May 2013.

[5] C. Chu and T. Jong, "A novel direct air-conditioning load control method," *IEEE Trans. Power Syst.*, vol. 23, no. 3, pp. 1356-1363, Aug. 2008.

[6] K. Huang and Y. Huang, "Integrating direct load control with interruptible load management to provide instantaneous reserves for ancillary services," *IEEE Trans Power Syst.*,vol.19, no.3, pp.1626-1634, Aug. 2004.

[7] Q. Jia, J. Shen, Z. Xu, and X. Guan, "Simulation-based policy improvement for energy management in commercial office buildings," *IEEE Trans. Smart Grid*, vol. 3, no. 4, pp. 2211-2223, Dec. 2012.

[8] H. Hao, A. Kowli, Y. Lin, P. Barooah, and S. Meyn, "Ancillary service for the grid via of commercial building HVAC systems," in *Proc. IEEE American Control Conf.*, pp. 467-472, June. 2013.

[9] M. Maasoumy, J. Ortiz, D. Culler, and A. S. Vincentelli, "Flexibility of commercial building HVAC fan as ancillary service for smart grid," in *Proc. IEEE Green Energy and Syst. Conf.*, Nov. 2013, page(s): 1-7.

[10] P. Zhao, G. P. Henze, S. Plamp, and V. J. Cushing, "Evaluation of commercial building HVAC systems as frequency regulation providers," *Energy and Buildings*, vol. 67, pp. 225-235, Dec. 2013.

[11] Y Lin, P. Barooah, and S. P. Meyn, "Low-frequency power-grid ancillary services from commercial building HVAC systems," in *Proc. IEEE Smart Grid Comm. Conf.*, pp. 169-174, Dec. 2013.

[12] J. D. Kelso, "2010 buildings energy data book", Energy Efficiency and Renewable Energy, U.S. Department of Energy, Mar. 2011.

[13] US Energy Information Administration, *Annual energy review 2011* (*DOE/EIA-0384*), [Online]. Available: www.eia.gov/totalenergy/data/ annual/pdf/aer.pdf

[14] A. M. García, F. Bouffard, and D. S. Kirschen, "Decentralized demand-side contribution to primary frequency control," *IEEE Trans. Power Syst.*, vol. 26, no. 1, pp. 411- 419, Feb. 2011.

[15] Z. Xu, J. Østergard, and M. Togeby, "Demand as frequency controlled reserve," *IEEE Trans. Power Syst.*, vol. 26, no.3, pp.1062- 1071,Aug. 2011.

[16] M. D. Galus, S. Koch, and G. Andersson, "Provision of load frequency control by phevs, controllable loads, and a cogeneration unit," *IEEE Trans. Ind. Electron.*, vol. 58, no. 10, pp. 4568- 4582, Oct. 2011.

[17] J. Kondoh, H. Aki, H. Yamaguchi, A. Murata, and I. Ishii, "Consumed power control of time deferrable loads for frequency regulation," in *Proc. IEEE PES Power Syst. Conf. Expo.*, New York, NY, Oct. 2004, page(s): 1-6.

[18] H. Milanda, R. Glöcknera, P. Taylor, R. JarleAaberg, and G. Hagen, "Load control of a wind-hydrogen stand-alone power system," *Intl. J. Hydrogen Energy*, vol. 31, no. 9, pp.1215-1235, Aug. 2006

[19] T. Masuta and A. Yokoyama, "Supplementary load frequency control by use of a number of both electric vehicles and heat pump water heaters," *IEEE Trans. Smart Grid*, vol. 3, no. 3, pp. 1253-1262, Sep. 2012.

[20] N. Lu, "An evaluation of the HVAC load potential for providing load balancing service," *IEEE Trans. Smart Grid*, vol. 3, no. 3, pp. 1263-1270, Sep. 2012.

[21] N. Lu and Y. Zhang, "Design considerations of a centralized load controller using thermostatically controlled appliances for continuous regulation reserves," *IEEE Trans. Smart Grid*, vol. 4, no. 2, pp. 914-921, June 2013.

[22] J. A. Short, D. G. Infield, and L. L. Freris, "Stabilization of grid frequency through dynamic demand control," *IEEE Trans. Power Syst.*, vol. 22, no. 3, pp. 1284-1293, Aug. 2007.

[23] J. Kondoh, N. Lu, and D. J. Hammerstrom, "An evaluation of the water heater load potential for providing regulation service," *IEEE Trans. Power Syst.*, vol. 26, no. 3, pp. 1309-1316, Aug. 2011.

[24] N. Shah, A. Phadke, and P. Waide, "Cooling the planet: opportunities for deployment of superefficient room air conditioners," Lawrence Berkeley National Laboratory, Apr. 2013.

[25] X. D. He, "Dynamic modeling and multivariable control of vapor compression cycles in air conditioning systems", Ph.D. thesis, Dept. of Mech. Eng., Massachusetts Inst. of Tech., Cambridge, MA, Feb. 1996.

[26] B.P. Rasmussen and A.G. Alleyne, "Dynamic modeling and advanced control of air conditioning and refrigeration systems", Air Conditioning and Refrigeration Center (ACRC TR-244), June 2006.

[27] S. Sanaye and M. Chahartaghi, "Thermal modeling and operating tests for the gas engine-driven heat pump systems", *Energy*, vol. 35, no. 1, pp.351-363, Jan. 2010.

[28] S. C. Kim, M. S. Kim, I. C. Hwang, and T. W. Lim, "Performance evaluation of a CO_2 heat pump system for fuel cell vehicles considering the heat exchanger arrangements", *Intl. J. Refrigeration*, vol. 30, no. 7, pp. 1195-1206, Nov. 2007

[29] U. K. Awan, "Experimental analysis of a variable capacity heat pump system equipped with vapour injection and permanent magnet motor", M.S. thesis, Dept. of Energy Tech., Royal Inst. of Tech., Stockholm, Sweden, Sep. 2012.

[30] T. Zakula, "Heat pump simulation model and optimal variable-speed control for a wide range of cooling conditions", M.S. thesis, Dept. of Arch., Massachusetts Inst. of Tech., Cambridge, MA, June 2010.

[31] J. L. Kirtley, *Electric power principles: sources, conversion, distribution, and use*, West Sussex, UK: John Wiley & Sons, 2010, pp. 306-313.

[32] *Copeland Scroll® Modular Compression: Variable Frequency Drives Modular Compression for Oil & Gas*, Aug. 2008, [Online]. Available: www.emersonprocess.com/en-us/Pages/Home.aspx, Emerson.

[33] *SMCTM-50 Technology and Control Advances: Sensorless Linear Acceleration and Energy Management*, [Online]. Available: http://literature.rockwellautomation.com/idc/groups/literature/documents/ wp/150-wp005_-en-p.pdf, Rockwell Automation.

[34] K. Bihler and D. Dominiak, *VLP Drive Software*, [Online]. Available: http://www.toshiba.com/ind/data/news/news_481.pdf, Toshiba

[35] *Variable Frequency Drives*, [Online]. Available: http://www.evapco.eu/sites/evapco.eu/files/white_papers/39-Variable-Frequency-Drives.pdf, Evapco.

[36] N. T. Gayeski, "Predictive pre-cooling control for low lift radiant cooling using building thermal mass", Ph.D. thesis, Dept. of Arch., Massachusetts Inst. of Tech., Cambridge, MA, Sep. 2010.

[37] T. Zakula, "Model predictive control for energy efficient cooling and dehumidification", Ph.D. thesis, Dept. of Arch., Massachusetts Inst. of Tech., Cambridge, MA, June 2013.

[38] X. Xu, S. Wang, "A simplified dynamic model for existing buildings using CTF and thermal network models," *Intl. J. Thermal Sciences*, vol. 47, no. 9, pp. 1249-1262, Sept. 2008.

[39] M. M. Gouda, S. Danaher, C.P. Underwood, "Building thermal model reduction using nonlinear constrained optimization," *Building and Environment*, vol. 37, no. 12, Dec. 2002.

[40] Y. J. Kim, L. K. Norford, and J. L. Kirtley Jr., "Analysis of a building power system with a rooftop PV array and PHEVs as an aggregator," *in Proc. IEEE PES Innovative Smart Grid Tech. Conf.*, Washington D.C., Feb. 2013, page(s):1-6.

[41] R. Krishnan, *Electric motor drives: modeling, analysis, and control*, New Jersey, US: Prentice Hall, 2001, pp. 492-502.
[42] P. Kunder, *Power System Stability and Control*, Toronto, CA: McGraw-Hill, 1994, pp. 581-626.
[43] L. Jiang, W. Yao, Q. H. Wu, J. Y. Wen, and S. J. Cheng, "Delay dependent stability for load frequency control with constant and time-varying delays", *IEEE Trans. on Power Sys.*, vol. 27, no. 2, pp. 932-941, 2012.
[44] X. Yu and K. Tomsovic, "Application of linear matrix inequalities for load frequency control with communication delay", *IEEE Trans. on Power Sys.*, vol. 19, no. 3, pp. 1508-1515, 2004.
[45] Y. G. Rebours, D. S. Kirschen, M. Trotignon, and S. Rossignol, "A survey of frequency and voltage control ancillary services—part I: technical features," *IEEE Trans. Power Syst.*, vol. 22, no. 1, pp. 350-357, Feb. 2007.
[46] Y. J. Kim, L. K. Norford, and J. L. Kirtley Jr., "Variable speed heat pump design for frequency regulation through direct load control," in *Proc. IEEE PES T&D Conf. Expo.*, Apr. 2014, page(s): 1-5.
[47] Weather History for KMACAMBR4, [Online]. Available: http://www.wunderground.com/weatherstation/WXDailyHistory.asp?ID=KMACAMBR4&month=7&day=21&year=2012, Weather Underground.
[48] Fast Response Regulation Signal, [Online]. Available: http://www.pjm.com/markets-and-operations/ancillary-services/mkt-based-regulation/fast-response-regulation-signal.aspx, PJM.
[49] IEEE distribution planning working group report, "Radial distribution test feeders," *IEEE Trans. Power Syst.*, vol. 6, no. 3, pp. 975-985, Aug. 1991
[50] Y. J. Kim, S. J. Ahn, P. I. Hwang, G. C. Pyo, and S. I. Moon, "Coordinated control of a DG and voltage control devices using a dynamic programming algorithm," *IEEE Trans. Power Syst.*, vol. 28, no. 1, pp. 42-51, Feb. 2013.
[51] M. F. M. Arani and E. F. El-Saadany, "Implementing virtual inertia in DFIG-based wind power generation," *IEEE Trans. Power Syst.*, vol. 28, no. 2, pp. 1373-1384, May 2013.

Young-Jin Kim (S'14) received his B.S. and M.S. degree in Electrical Engineering from Seoul National University in 2007 and 2010, respectively, and worked for Korea Electric Power Corporation (KEPCO) as a power transmission and distribution system engineer from 2007 to 2011.

He is a Ph.D. candidate in Electrical Engineering at Massachusetts Institute of Technology (MIT). His research fields of interest include distributed generators, renewable energy resources, and smart buildings. He receives the Samsung Scholarship for Ph.D. degree students.

Leslie K. Norford received the B.S. degree in Engineering Science from Cornell University in 1973 Ph.D. degree in mechanical and aerospace engineering from Princeton University, Princeton, NJ, in 1984. He is currently a Professor of Building Technology in the Department of Architecture, Massachusetts Institute of Technology.

He is the Lead Investigator of the Center for Environmental Sensing and Modeling, an interdisciplinary research group in the Singapore-MIT Alliance for Research and Technology, Singapore. His current research interests include monitoring the performance of mechanical and electrical equipment in buildings, optimization techniques as applied to design and operation of buildings and their mechanical systems, and measurements and simulations of interaction of buildings and urban environments.

James L. Kirtley Jr. (S'69–M'71–SM'80–F'91–LF'11) received the Ph.D. degree in electrical engineering from the Massachusetts Institute of Technology (MIT), Cambridge, MA, USA, in 1971. He has been a member of the faculty of the Department of Electrical Engineering and Computer Science, MIT, since 1971, where he is currently Professor of Electrical Engineering.

He was also an Electrical Engineer with the Large Steam Turbine Generator at General Electric, General Manager and Chief Scientist with SatCon Technology Corporation, and was Gastdozent at the Swiss Federal Institute of Technology. He is a specialist in electric machinery and electric power systems. He is a member of the Editorial Board of the Journal Electric Power Components and Systems. Prof. Kirtley is a Registered Professional Engineer in Massachusetts. He is a member of the U.S. National Academy of Engineering. He was awarded the Nikola Tesla Prize in 2002 and the IEEE Third Millennium Medal. He was Editor-in-Chief of the IEEE Transactions on Energy Conversion from 1998 to 2006 and continues to serve as Editor for that journal.